Hindawi
International Journal of Energy Research
Volume 2023, Article ID 4418741, 16 pages
https://doi.org/10.1155/2023/4418741

WILEY | Hindawi

Research Article

Fault Detection and Classification to Design a Protection Scheme for Utility Grid with High Penetration of Wind and Solar Energy

Abhishek Gupta,[1] Ramesh Kumar Pachar,[1] Om Prakash Mahela ,[2,3] and Baseem Khan [3,4]

[1]*Department of Electrical Engineering, Swami Keshvanand Institute of Technology, Management & Gramothan, Jaipur, India*
[2]*Power System Planning Division, Rajasthan Rajya Vidyut Prasaran Nigam Limited, Jaipur, India*
[3]*Department of Project Management, Universidad Internacional Iberoamericana, Campeche C.P. 24560, Mexico*
[4]*Department of Electrical and Computer Engineering, Hawassa University, Hawassa, Ethiopia 05*

Correspondence should be addressed to Baseem Khan; baseem.khan1987@gmail.com

Received 1 September 2022; Revised 19 February 2023; Accepted 7 April 2023; Published 28 April 2023

Academic Editor: Akshay Kumar Saha

Copyright © 2023 Abhishek Gupta et al. This is an open access article distributed under the Creative Commons Attribution License, which permits unrestricted use, distribution, and reproduction in any medium, provided the original work is properly cited.

This paper designed a protection scheme for utility grid with high share of renewable energy (RE) generated from wind energy and solar energy plants. This is based on extraction of features from the current using Stockwell transform (ST), Hilbert transform (HT), and alienation coefficient. A Stockwell index (SI) is designed by extracting current features using ST, a Hilbert index (HI) is designed by extracting current features using HT, and an alienation index (AI) is designed by extracting current features using an alienation coefficient. A fault index (FI) is formulated by multiplying the SI, HI, AI, and WF (weight factor). This FI is implemented for fault detection. Fault classification is achieved considering number of fault phases and ground fault index (GFI). This GFI is designed by processing zero sequence currents applying ST. GFI effectively identifies the ground involved during event of a fault. A designed protection scheme is effective to identify faults in the scenario of high RE share and during various cases of study which includes the variations of fault impedance, different fault occurrence angles (FOA), fault incident at different nodes, and noisy condition. This protection scheme effectively discriminates the fault events from the operational events such as feeder operation, load, and capacitor switching. Performance of hybrid protection method formulated in this paper is better relative to alienation coefficient-based protection scheme (ACPS) reported in literature. The ACPS has maximum error and mean error of fault detection equal to 9.54% and 5.99%, respectively, which is relatively high compared to the respective values for the proposed method which are 1.89% and 0.978%, respectively. ACPS is effective for detecting the fault events in noise level of 30 dB SNR (signal-to-noise ratio) whereas the proposed method effectively identifies the faults in the high noise scenario of 20 dB SNR.

1. Introduction

Recent concerns of environmental issues, fossil fuel problems, and risks of energy security have forced all the countries for focusing to increase the use of renewable energy (RE). This has motivated the utilities to increase level of RE in the grids [1]. The variable and uncertain nature of these RE sources have posed challenges to the utility network operators in terms of grid security, power system protection, power quality, energy management, and flexibility. The application of machine learning (ML), signal processing, deep learning (DL), and intelligent techniques have solved protection problems. An ensemble deep learning approach (EDLA) is designed by the authors of [2] for fault detection for the utility grid network to support the automation, validation, and overfitting. In [3], the authors formulated a wavelet transform (WT) powered fault detection method which is implemented for providing protection to a transmission line with availability of a wind turbine. The protection scheme supports effective protection but performance is degraded

with high level noise. An in-depth study for evaluating the effect of wind and solar energy injection on the performance of distance protection of a transmission line is presented in [4]. Further, different relay settings have been suggested for different penetration levels of RE. Impact of RE penetration levels on zones of fault locations is also investigated. In [5], the authors detailed a study of existing approaches and practices for fault detection, categorization, and location on a distribution network. Different techniques, their advantages, disadvantages, and application for distribution grids, smart grids, and microgrids have been discussed in detail. A comparative study is also presented which helps to select a particular method for specific application. A brief review of techniques for fault diagnosis in microgrids with high contribution of solar energy is discussed in [6]. A method consisting of Hilbert–Huang transform (HHT) and decision tree to detect islanding condition as well as fault events incident on a distribution network with RE penetration is designed by authors in [7]. This method is also effective to classify and localize the fault events. It also effectively discriminates the fault and islanding events from the switching transients. In [8], authors designed a protection mechanism for a low-voltage AC microgrids dominated by inverters to detect the low impedance faults using direction of active power flows, magnitude of current, and voltage sags. It is established that developed protection strategy is effective to provide protection to the microgrid of all topology, configuration, and operational mode. A protection scheme for fault detection using a data-driven approach and fault classification using the Gaussian regression method is designed for smart AC microgrid in [9]. The study is validated using the IEEE-15 node network (distribution system) having integrated solar photovoltaic (PV) distributed generator (DG). In [10], the authors presented a study for detection of fault incident on a network of integrated energy system by application of machine learning- (ML-) based techniques. The algorithm has achieved the accuracy of 98.67%. The fault recognition methods are reported in [11–14]. An optimal design of a nonfragile proportional–integral–derivative (PID) controller for an automatic voltage regulator (AVR) to address the challenge presented by uncertainties in the plant model parameters and perturbations in the controller gains to improve stability and controller nonfragility at the same time is reported in [15]. This method has low computational complexity and achieves fast convergence rate because it utilized both local and global search techniques. In [16], the authors designed a decomposition supported multiobjective resilient control for blade pitch of a wind energy conversion system (WECS) to achieve better damping capability with minimum oscillation, settling time, and overshoot. This is established that proposed technique achieved the damping with minimum overshoot around 2.2329% and settling time around 9.2626 which is superior compared to meta-heuristics techniques. In [17], the authors designed a direct current (DC) charging station with bipolar properties for a microgrid system to convert a two-wire system into three wires with a neutral line. This is capable of handling different output loads where neutral-line voltage is effective and dynamic performance is improved relative to a traditional controller. Fuzzy logic (FL) and Harris hawks optimization (HHO) techniques for energy management system (EMS) using modified cost function are introduced in [18]. These methods achieved the optimal performance of seawater desalination plants (SWDP) with minimum feed-in-tariff. However, the performance of the method is affected due to variation of energy price with time and uncertainties of system parameters. An optimization technique based on use of equilibrium optimizer for dynamic cutting force coefficients of the end-milling process [19] and improved bald eagle search algorithm with dimension learning supported hunting for autonomous vehicle considering vision dynamics [20] are also reported in literature.

Review of existing and above discussed literature indicates that simultaneous use of signal processing methods can be used to design protection scheme with improved performance for detection and classifying the fault conditions incident on a utility network with high share of RE. Main research contributions of this paper are mentioned below:

(i) This paper designed a scheme for protection of utility grid against faulty condition with availability of high share of RE which uses the feature extracted from currents applying the ST, HT, and alienation coefficient

(ii) A SI is designed extracting current features using ST, a HI is designed extracting current features using HT, and an AI is designed extracting current features using the alienation coefficient. SI, HI, AI, and WF are multiplied for computing the FI. FI is implemented for fault detection

(iii) Fault classification is achieved applying number of fault phases along with GFI. This GFI is formulated by processing zero sequence currents applying the ST. GFI effectively identifies ground involved during fault event

(iv) Designed protection scheme effectively recognize the faults with high share of RE and during different case studies

(v) Performance of designed protection method is superior relative to the alienation coefficient-based protection scheme with respect to mean error of fault detection and applicability of algorithm for different scenarios of the power system

Structuring of this paper includes the seven sections. Introduction and research findings are described in the Section 1. The test network of utility grid with details of wind energy plant and solar energy plant are discussed in Section 2. The design of the protection method including fault detection approach and fault classification approach are discussed in Section 3. Section 4 describes the results of simulation to detect and classify faults. Validation of the algorithm using different case studies is discussed in Section 5. Section 6 includes the performance comparative discussion. Conclusions are included and discussed in Section 7.

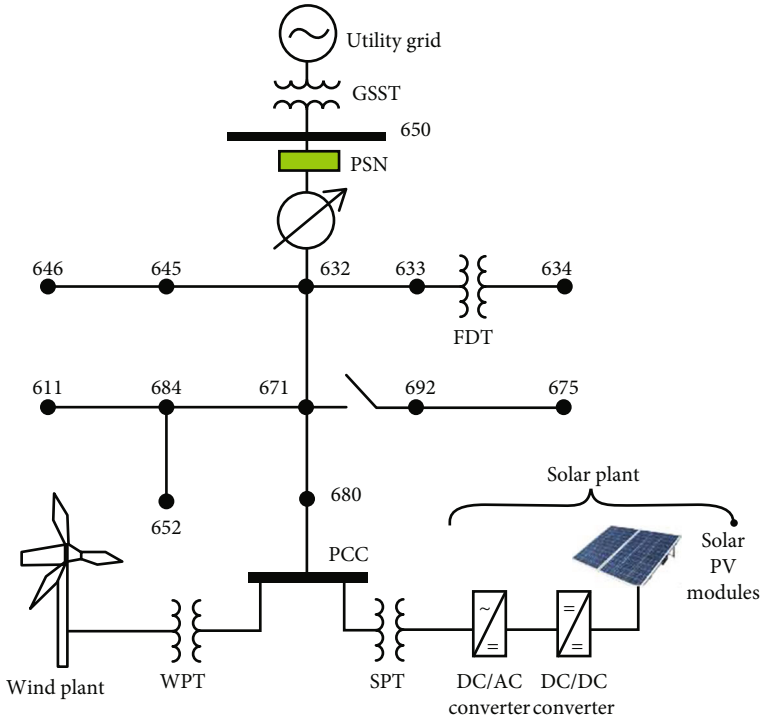

Figure 1: Wind energy and solar energy plants connected to the IEEE-13 node test network.

2. Test System

A test network for validation of the designed protection scheme is realized by integrating a solar energy plant (SEP) rated at 1 MW and a wind energy plant (WEP) rated at 1.5 MW on a 680-numbered node of an IEEE-13 node test feeder as illustrated in Figure 1. Therefore, the total capacity of RE generators is 2.5 MW. Details and technical parameters of load, feeder, capacitor, and transformer available in [21] are utilized for this study. SEP and WEP are connected to the 680-numbered node of the test network through solar plant transformer (SPT) and wind plant transformer (WPT), respectively. SEP and WEP generate power at 0.270 kV and 0.575 kV voltage levels, respectively. A feeder transformer (FDT) is used to operate node 634 on 0.48 kV, and all other nodes operate on 4.16 kV. A grid substation transformer (GSST) is used for connecting a test feeder to a large network of utility which is operated at 115 kV. The total load connected to the test feeder amounts to 5 MVA. Hence, MVA rating of the test feeder is 5 MVA. A RE capacity of 2.5 MW is connected to the test feeder against the 5 MVA rating; hence, RE penetration level of 50% is achieved. The proposed fault recognition method effectively detects all types of fault events under the condition of 50% RE penetration level. Technical parameters of solar plates and converters used in this study are available in [22]. Similarly, technical parameters of wind turbine and converters used in this study are available in [23]. The 650-numbered node is taken as a protection scheme node (PSN) where currents are recorded for analysis using protection approach. The IEEE-13 bus test network is a radial feeder fed from the node 650 which is integrated to the utility grid. Hence, the protection scheme equipped at this node will provide protection to the complete feeder. Hence, node 650 is considered to install the protection scheme. All the elements of distribution system used for the study are deterministic in nature which means that the behavior of the elements such as feeders, loads, capacitors, and generator is well-defined. The nature of the system voltage and current in the elements is sinusoidal in nature. The proposed protection method detects the changes observed in the current waveform from the sinusoidal nature during fault event. Hence, model constraints are not dynamic in nature rather all limitations of model are static in nature.

3. Proposed Methodology

The fault detection and categorization approach used to design scheme for protection of the utility network against fault events in the availability of high share of RE generation (wind and solar) is described in this section.

3.1. Fault Detection. Schematic diagram including all steps for detection of fault events is elaborated in Figure 2. All steps and indexes used to design a fault index (FI) to detect the faults incident on power network are elaborated in the below subsections.

3.1.1. Hilbert Index. Hilbert transform is applied to process the current waveform ($i(t)$) at sampling frequency of 3.84 kHz with the help of the below detailed mathematical formulation and output matrix $H(i(t))$ is computed [24].

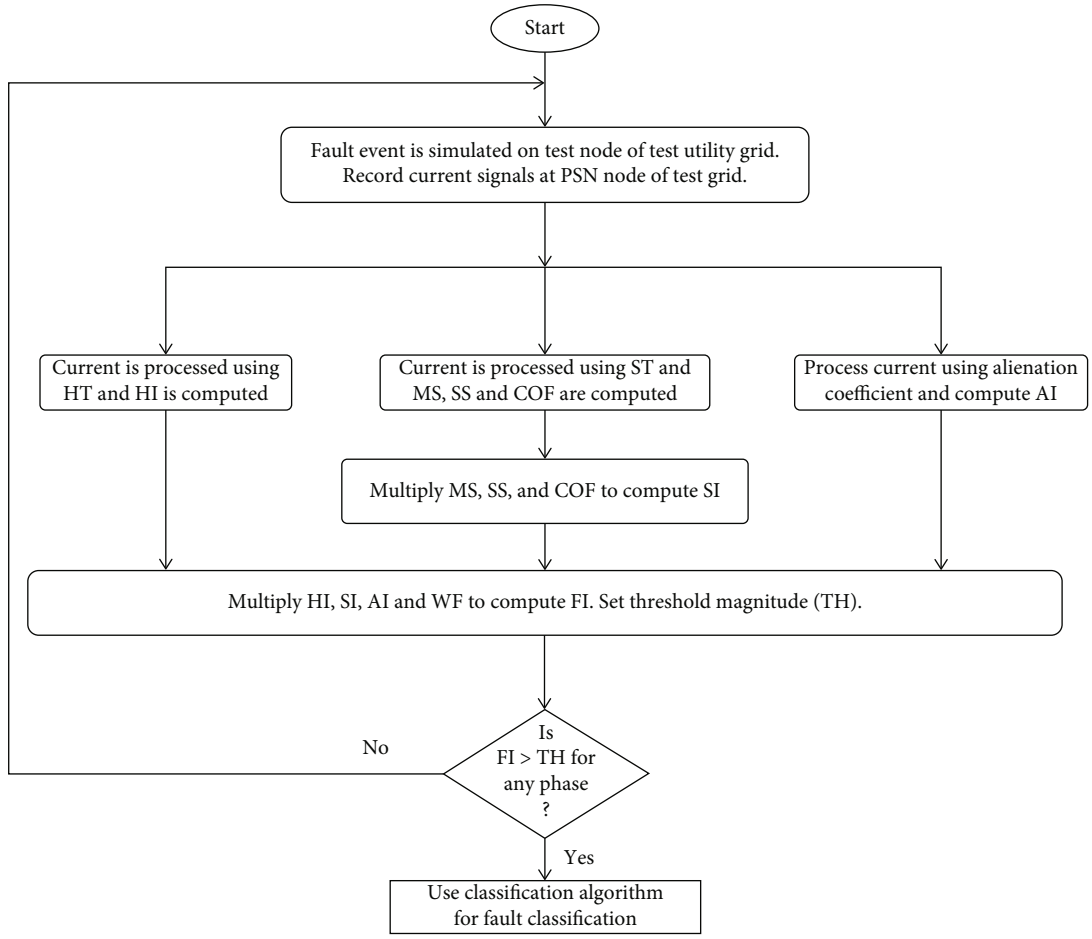

Figure 2: Fault detection approach.

$$H(i(t)) = \frac{1}{\pi}\mathrm{PV}\int_{-\infty}^{\infty}\frac{i(\tau)}{t-\tau}d\tau. \quad (1)$$

Here, PV is the principle quantity for Cauchy's integral, τ is the time period, t is the momentary time, and $H(i(t))$ is the matrix of HT output. The Hilbert index (HI) is designed by taking absolute magnitudes of matrix $H(i(t))$ which is a row matrix.

$$\mathrm{HI} = \mathrm{abs}(H(i(t))). \quad (2)$$

3.1.2. Stockwell Index. Stockwell index (SI) is applied to decompose the current using ST, and the output matrix having absolute magnitudes (STOMA) is obtained as detailed below [25]:

$$\mathrm{STOMA} = \mathrm{abs}\left(\int_{-\infty}^{\infty} i(t)\frac{|f|}{\sqrt{2\pi}}e^{-\left(f^2(\tau-t)^2\right)/2}e^{-j2\pi ft}dt\right). \quad (3)$$

Median of STOMA (MST) is computed as detailed below:

$$\mathrm{MST} = \mathrm{median}(\mathrm{STOMA}). \quad (4)$$

Summation of all elements of column matrix of STOMA (SST) is computed as detailed below:

$$\mathrm{SST} = \mathrm{sum}(\mathrm{STOMA}). \quad (5)$$

Covariance of SST (COFT) is computed as detailed below:

$$\mathrm{COFT} = \mathrm{sum}(\mathrm{SST}). \quad (6)$$

The Stockwell index is computed by multiplication of MST, SST, and COFT as detailed below:

$$\mathrm{SI} = \mathrm{MST} \times \mathrm{SST} \times \mathrm{COFT}. \quad (7)$$

3.1.3. Alienation Index. The current variables i_1 and i_2 are considered at quarter cycle time difference to compute correlation coefficient (CRC) as described below:

$$\mathrm{CRC} = \frac{N_s\sum i_1 i_2 - (\sum i_1)(\sum i_2)}{\sqrt{\left[N_s\sum i_1^2 - (\sum i_1)^2\right]\left[N_s\sum i_2^2 - (\sum i_2)^2\right]}}. \quad (8)$$

Here, N_s is the number of samples of a cycle, i_1 is the current samples at time t_0, i_2 is the current samples at $-T + t_0$ time, and T is the time period of the current cycle.

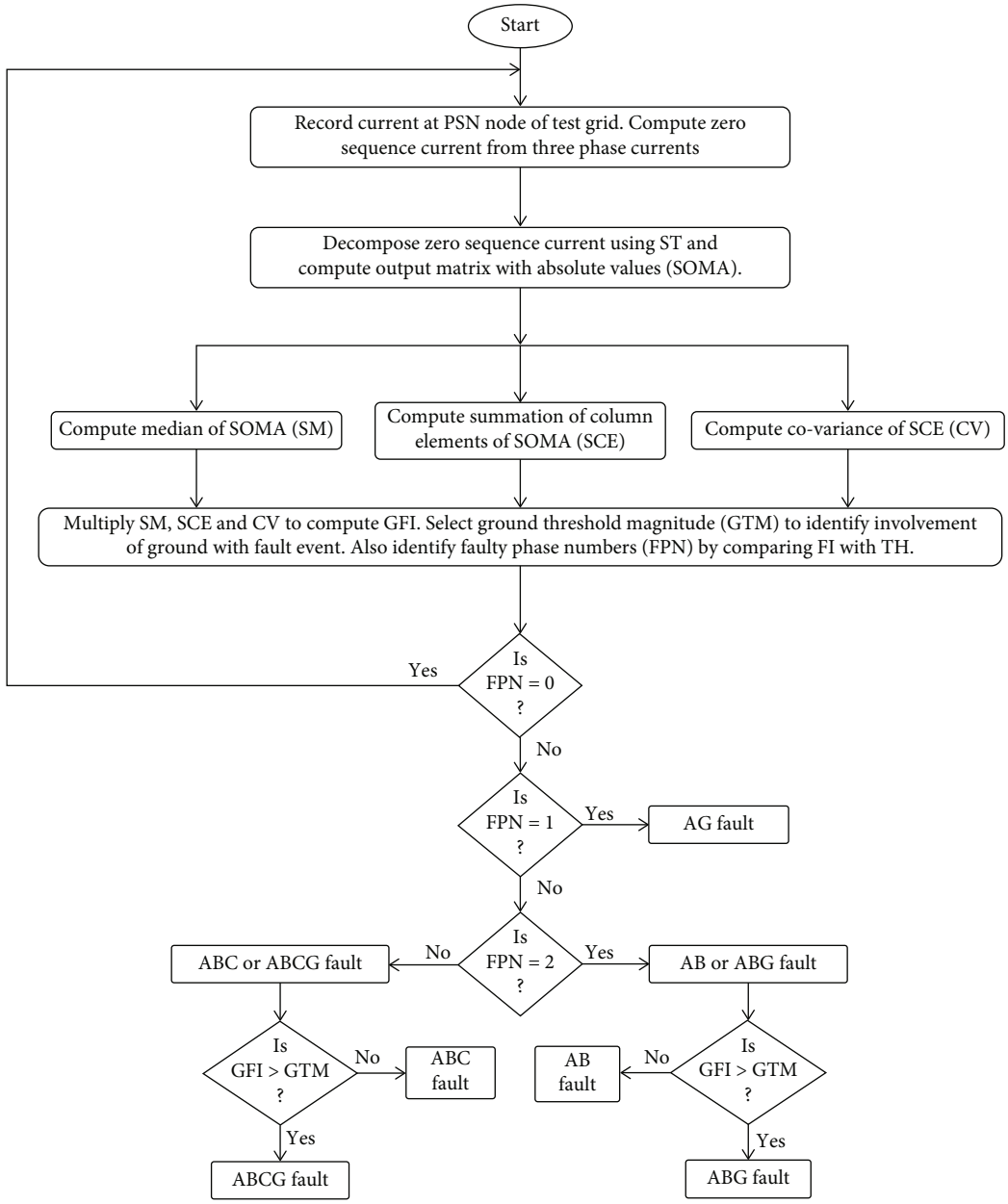

Figure 3: Fault classification approach.

The alienation index (AI) is computed using CRC by the below detailed mathematical formulation:

$$\mathrm{AI} = 1 - \mathrm{CRC}^2. \tag{9}$$

3.1.4. Fault Index. The FI is formulated by multiplying the HI, SI, AI, and a weight factor (WF). WF is assigned a value of 5000 for this study. This value of WF is selected after testing the approach on different cases of study which include variations of fault impedance, fault occurrence angle (FOA), different fault occurrence nodes (FON), and operational events. A threshold (TH) magnitude of 20,000 is decided to discriminate the fault event from the healthy events. During fault events, the magnitude of FI becomes greater compared to the TH and during the conditions of healthy scenario the FI magnitude is low relative to TH. Again TH magnitude is finalized by testing algorithm for various case of study like variations of fault impedance, fault occurrence angle (FOA), different fault occurrence nodes (FON), and operational events.

$$\mathrm{FI} = \mathrm{HI} \times \mathrm{SI} \times \mathrm{AI} \times \mathrm{WF}. \tag{10}$$

3.2. Fault Classification. The fault classification algorithm is illustrated in Figure 3. Fault classification is established considering the numbers of faulty phase and a ground fault index (GFI). GFI helps in detecting the ground involved during a fault condition. Computation of GFI is described in below subsections.

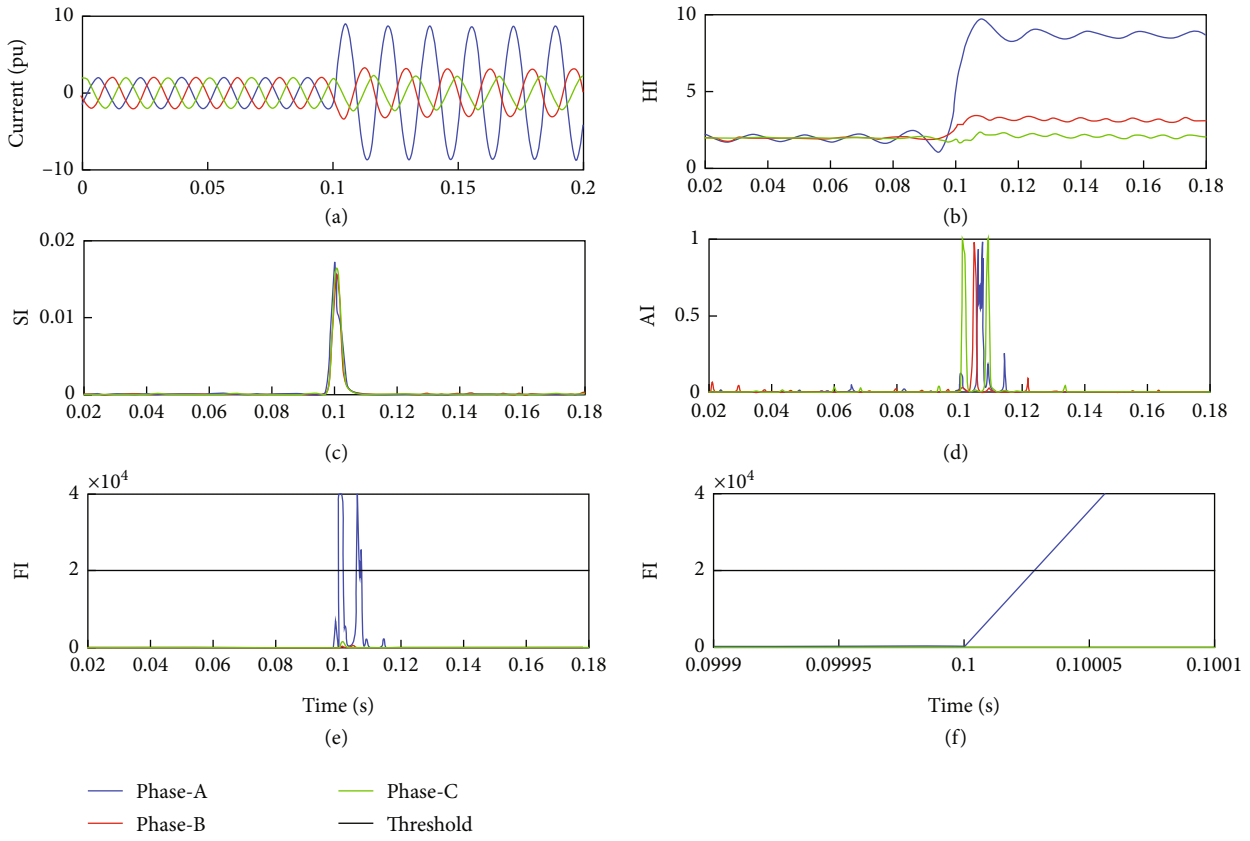

Figure 4: AG fault condition: (a) phase current waveforms, (b) HI, (c) SI, (d) AI, (e) FI, and (f) high-resolution FI plot.

3.2.1. Ground Fault Index. The zero sequence current is decomposed by the application of ST, and GFI is computed. The following are steps to compute the GFI:

(i) Current of zero sequence (I_0) is computed using the currents associated with all three phases as described below:

$$I_0 = \frac{(I_1 + I_2 + I_3)}{3} \tag{11}$$

(ii) Process I_0 applying the ST and compute output matrix with absolute values (SOMA)

(iii) Compute median of SOMA (MS) as described below:

$$\text{MS} = \text{median}(\text{SOMA}) \tag{12}$$

(iv) Compute summation of column elements of SOMA(SCE) as described below:

Table 1: Time for detection of faults by the use of PSM.

S. no.	Fault category	Fault identification time (s)
1	AG	10^{-5} s
2	AB	5×10^{-6} s
3	ABG	3×10^{-6} s
4	ABC	10^{-6} s
5	ABCG	10^{-6} s

$$\text{SCE} = \text{sum}(\text{SOMA}) \tag{13}$$

(v) Compute covariance of SCE (COF) as described below:

$$\text{COF} = \text{covar}(\text{SCE}) \tag{14}$$

(vi) Compute GFI using multiplication of MS, SCE, and COF as detailed below:

$$\text{GFI} = \text{MS} \times \text{SCE} \times \text{COF} \tag{15}$$

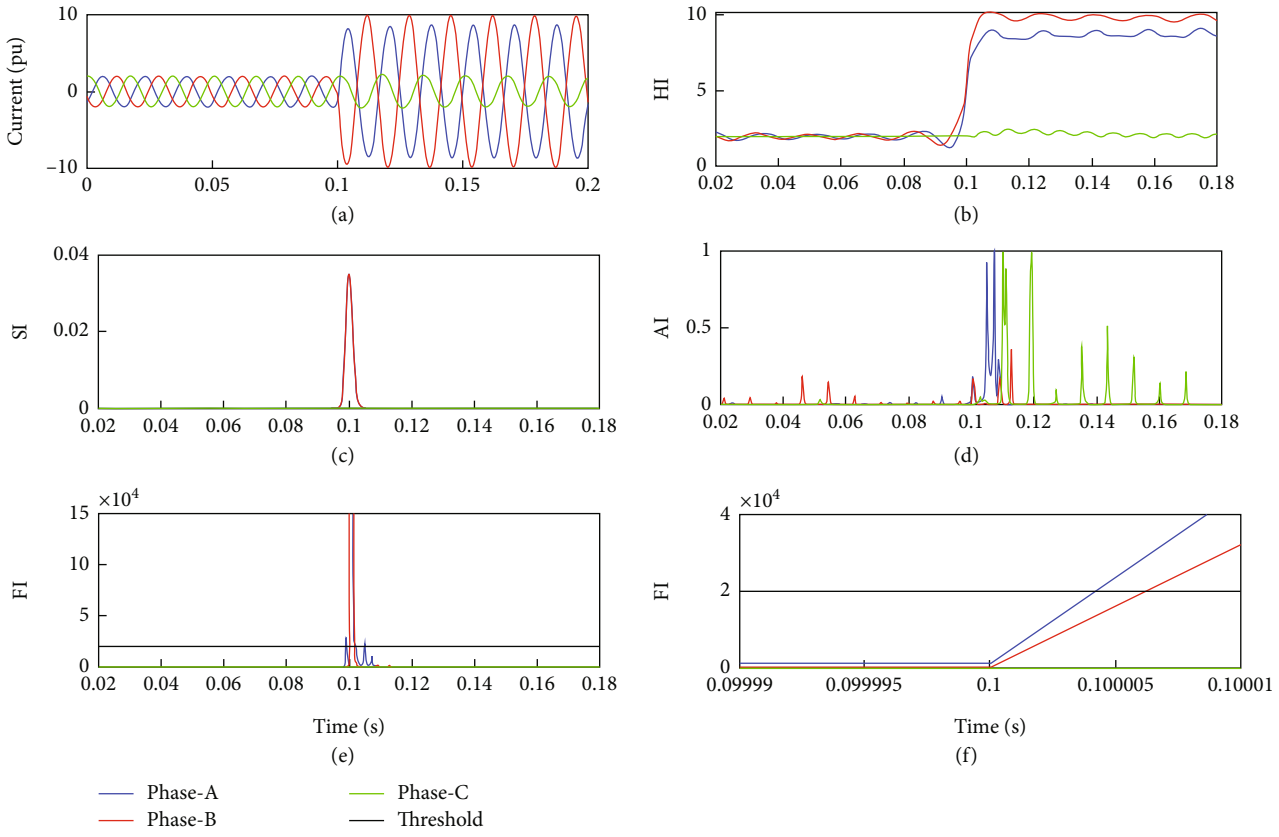

Figure 5: AB fault: (a) currents, (b) HI, (c) SI, (d) AI, (e) FI, and (f) high-resolution FI plot.

A ground threshold magnitude (GTM)) of 50 is decided for investigating the ground involved during a fault condition. This value of GTM is selected by testing the approach for various case studies like variations of fault impedance, fault occurrence angle (FOA), different fault occurrence nodes (FON), and operational events.

3.3. Tuning of Parameters. All parameters of the protection algorithm for fault detection and classification have been adjusted using a hit and trial approach by testing the algorithm on 25 data sets of each fault event. Parameters for which highest accuracy is obtained are considered for the method. It is established that parameters considered resulted in accuracy of algorithm higher than 99%.

4. Discussion of Simulation Results

The simulation results for detection of fault conditions associated with utility grid network having 50% RE power (solar and wind) injection are discussed in this section. The faults include phase-A to ground (AG), phase-A and phase-B (AB) fault, phase-A and phase-B with ground (ABG) fault, three-phase fault (ABC), and three-phase fault with ground (ABCG).

4.1. AG Fault. An AG fault occurs on node 671 of the utility system. Currents pertaining to all phases are measured at PSN and illustrated in Figure 4(a). Currents are analyzed by application of the designed protection approach to compute HI, SI, AI, and FI which are shown in Figures 4(b)–4(e) sequentially. A high-resolution FI plot is depicted in Figure 4(f). Time in which the AG fault has been identified is provided in Table 1.

This is seen in Figure 4(a) that current associated with faulty phase-A is increased just after fault occurrence. However, current associated with healthy phases-A and B change by small quantum. Figure 4(b) details that HI of phase-A is increased due to AG fault. However, deviations in magnitude of HI for phases-A and B (healthy in nature) is small. Figure 4(c) details that SI corresponding to every phase has become high because of fault occurrence. Figure 4(d) shows that AI pertaining to every phase has increased because of AG fault occurrence at 0.1 s. Figure 4(e) describes that FI of faulty phase-A is increased due to AG fault occurrence at 0.1 s and crossed the TH. However, FI for healthy phases-A and B remains below TH. Figure 4(f) gives an indication that FI pertaining to phase-A has become higher relative to TH in time interval of 10^{-5} s which indicates that protection algorithm is fast to detect AG fault.

4.2. AB Fault. Fault which includes phases-A and B and not the ground (AB) is simulated to occur on 671-numbered node of utility system. Currents of all phases are recorded at PSN (node 650) and illustrated in Figure 5(a). These currents are analyzed using the designed protection approach for computing HI, SI, AI, and FI which are shown in

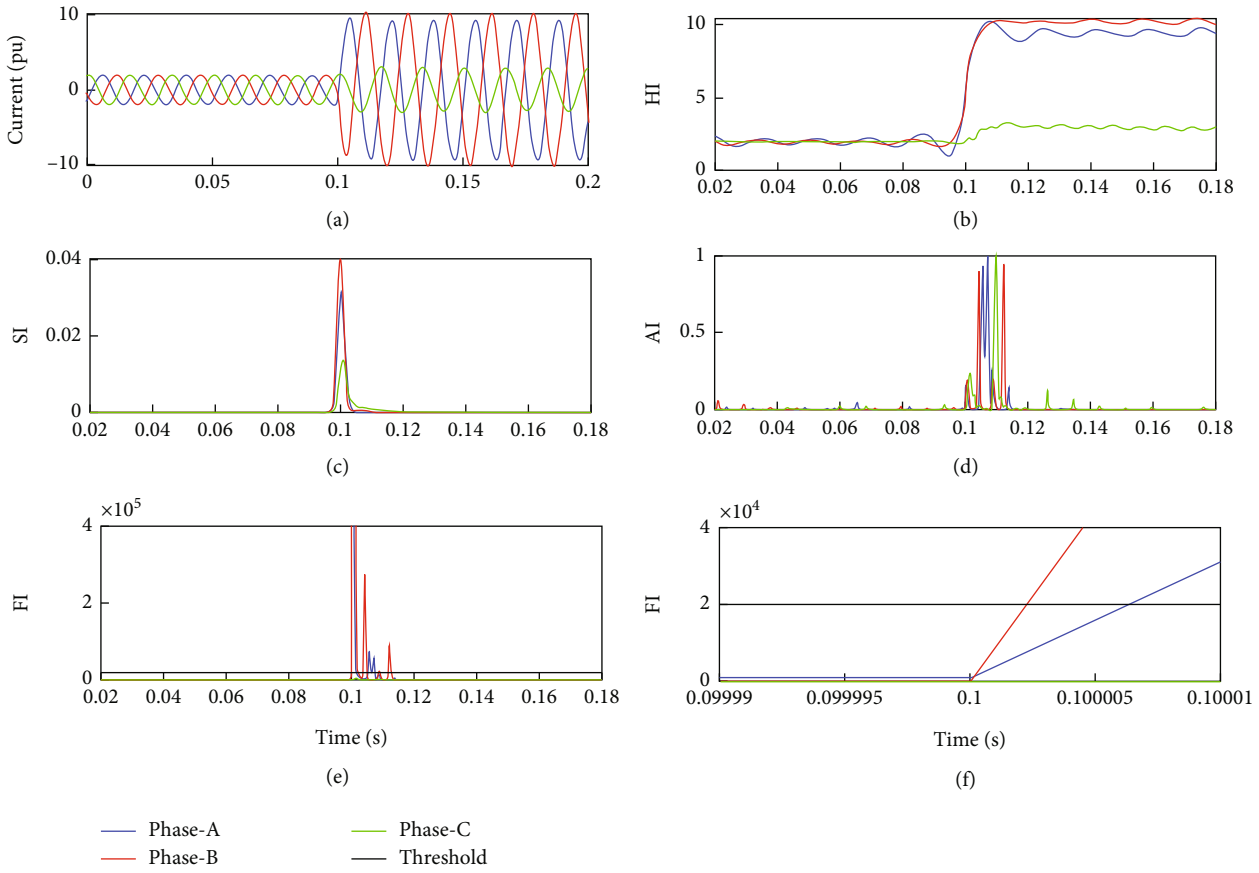

Figure 6: ABG fault: (a) currents, (b) HI, (c) SI, (d) AI, (e) FI, and (f) high-resolution FI plot.

Figures 5(b)–5(e) sequentially. A high-resolution FI plot is depicted in Figure 5(f). Time in which the AB fault has been identified is provided in Table 1.

This is seen in Figure 5(a) that current of phases-A and B (faulty in nature) has increased after fault incidence. However, current of healthy phase-C changes by small quantum. Figure 5(b) shows that HI of phases-A and B (faulty in nature) has become high due to AB fault. However, change in the magnitude of HI associated to phase-C (healthy nature) is small. Figure 5(c) depicts that SI corresponding to phases-A nd B has become high because of fault incidence. However, the SI of phase-C remains near to zero. Figure 5(d) shows that AI associated with every phase has become high because of AB fault occurrence at 0.1 s. Figure 5(e) details that FI associated to phases-A and B has become high due to AB fault occurrence at 0.1 s and crossed the TH. However, FI for healthy phase-C remains below TH. Figure 5(f) describes that FI associated to phases-A and B has become high in comparison to TH in time interval of 5×10^{-6} s which indicates that the protection algorithm is fast to detect AB fault.

4.3. ABG Fault. Fault incident on phases-A and B with ground (ABG) is simulated to occur on the 671-numbered node of the utility system. Currents of all phases are recorded at PSN (node 650) and illustrated in Figure 6(a). Currents are analyzed by application of the designed protection approach to compute HI, SI, AI, and FI which are shown in Figures 6(b)–6(e) sequentially. A high-resolution FI plot is depicted in Figure 6(f). Time in which the ABG fault has been identified is provided in Table 1.

This is seen in Figure 6(a) that current associated to phases-A and B has become high after fault incidence. However, current of healthy phase-C changes by small quantum. Figure 6(b) describes that HI of phases-A and B (faulty in nature) has become high due to ABG fault. However, change in HI magnitude for phase-C (healthy nature) is small. Figure 6(c) depicts that SI associated to all phases has become high due to fault incidence. Figure 6(d) shows that AI associated to all phases has become high due to ABG fault occurrence at 0.1 s. Figure 6(e) details that FI of faulty phases-A and B has become high due to ABG fault occurrence at 0.1 s and crossed the TH. However, FI for healthy phase-C remains below TH. Figure 6(f) shows that FI associated with phases-A and B has become high relative to TH in time interval of 3×10^{-6} s which indicates that protection algorithm is fast to detect ABG fault.

4.4. ABC Fault. Fault which includes all phases but not ground (ABC) is simulated to occur on 671-numbered node of the utility system. Currents of all phases are measured at PSN and illustrated in Figure 7(a). Currents are analyzed by application of the designed protection approach to compute HI, SI, AI, and FI which are shown in Figures 7(b)–7(e)

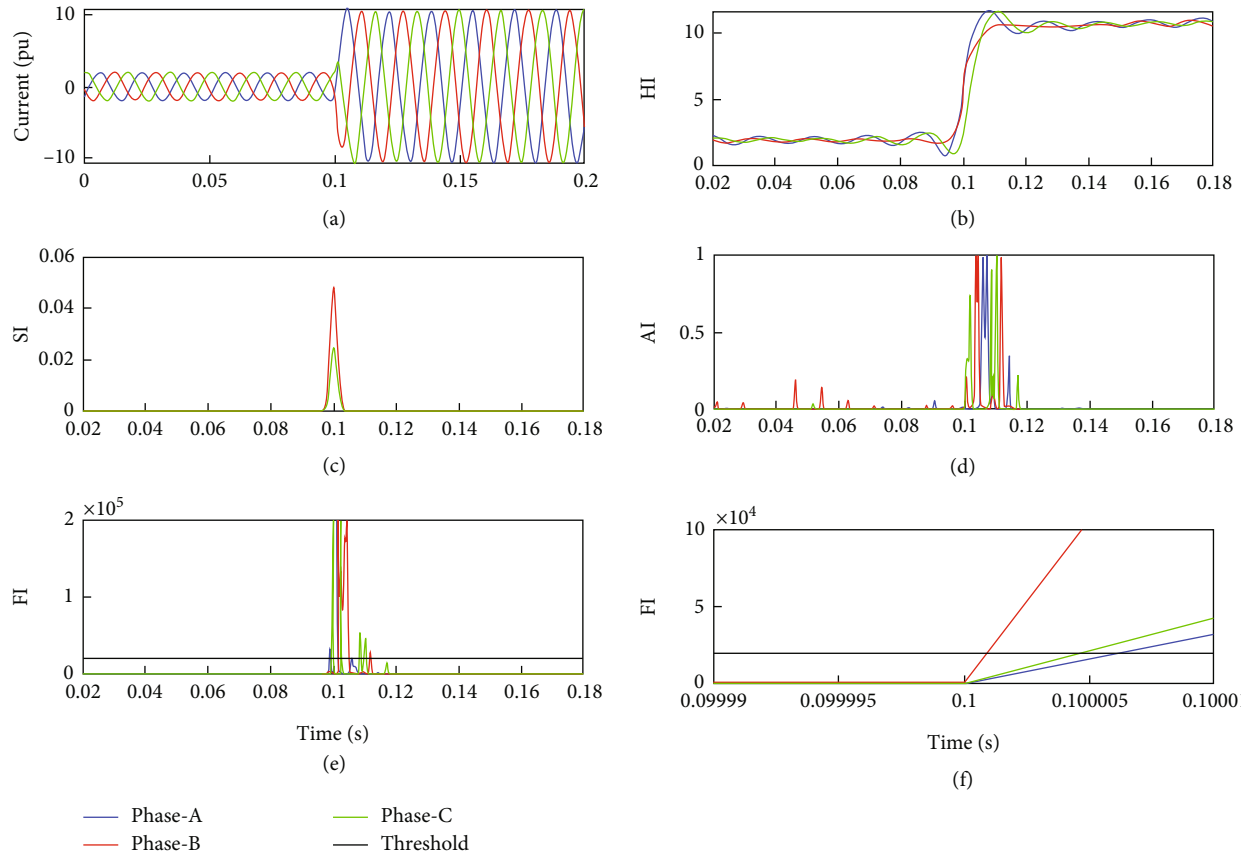

Figure 7: ABC fault: (a) current waveforms, (b) HI, (c) SI, (d) AI, (e) FI, and (f) high-resolution FI plot.

sequentially. A high-resolution FI plot is depicted in Figure 7(f). Time in which the ABC fault has been identified is provided in Table 1.

This is seen in Figure 7(a) that current associated to every faulty phase has become high after fault incidence. Figure 7(b) details that HI of every faulty phase has become high due to ABC fault. Figure 7(c) depicts that SI of all phases has become high due to fault incidence. Figure 7(d) shows that AI of all phases has become high due to ABC fault occurrence at 0.1 s. Figure 7(e) details that FI of all faulty phases is increased due to ABC fault occurrence at 0.1 s and crossed the TH. Figure 7(f) details that FI for all phases has become high in comparison to TH in time interval of 10^{-6} s indicating that protection algorithm is fast to detect ABC fault.

4.5. ABCG Fault. Fault which includes all phases and also ground (ABCG) is simulated to occur on node 671 of the utility system. Currents pertaining with all phases are measured at PSN and illustrated in Figure 8(a). These currents are processed by applying the designed protection approach to compute HI, SI, AI, and FI which are shown in Figures 8(b)–8(e) sequentially. A high-resolution FI plot is depicted in Figure 8(f). Time in which the ABCG fault has been identified is provided in Table 1.

This is seen in Figure 8(a) that current associated to all faulty phases has become high after ABCG fault incidence. Figure 8(b) details that HI of all faulty phases has become high due to ABCG fault. Figure 8(c) depicts that SI of every phase has become high due to ABCG fault incidence. Figure 8(d) shows that AI of every phase has increased due to ABCG fault occurrence at 0.1 s. Figure 8(e) shows that FI of all faulty phases has increased due to ABCG fault occurrence at 0.1 s and crossed the TH. Figure 8(f) details that FI for all phases has become high in comparison to TH in time interval of 10^{-6} s indicating that protection algorithm is fast to detect ABCG fault.

4.6. Fault Classification. Faults are classified using faulty phase numbers and GFI. Faults involving only one phase and ground (AG, BG, and CG) is incident when only one phase becomes faulty. Peak magnitude of FI pertaining with all phases during investigated fault events are provided in Table 2. Two faulty phase indicates the presence of two phase fault which does not involves ground (AB, BC, and AC) or two phase fault which involves ground (ABG, BCG, and ACG). Three faulty phase indicates availability of fault on all three phases but not ground (ABC) or fault on three phases and also ground (ABCG). Availability of ground with a fault is identified using GFI. The GFI for AB and ABG faults is demonstrated in Figure 9. This is recognized that the peak of GFI is high relative to GTM (50) during the ABG fault due to availability of ground and low relative to GTM for AB fault. Hence, AB and ABG faults are differentiated from each other accurately. In the similar way, ground involvement with a three-phase fault can also

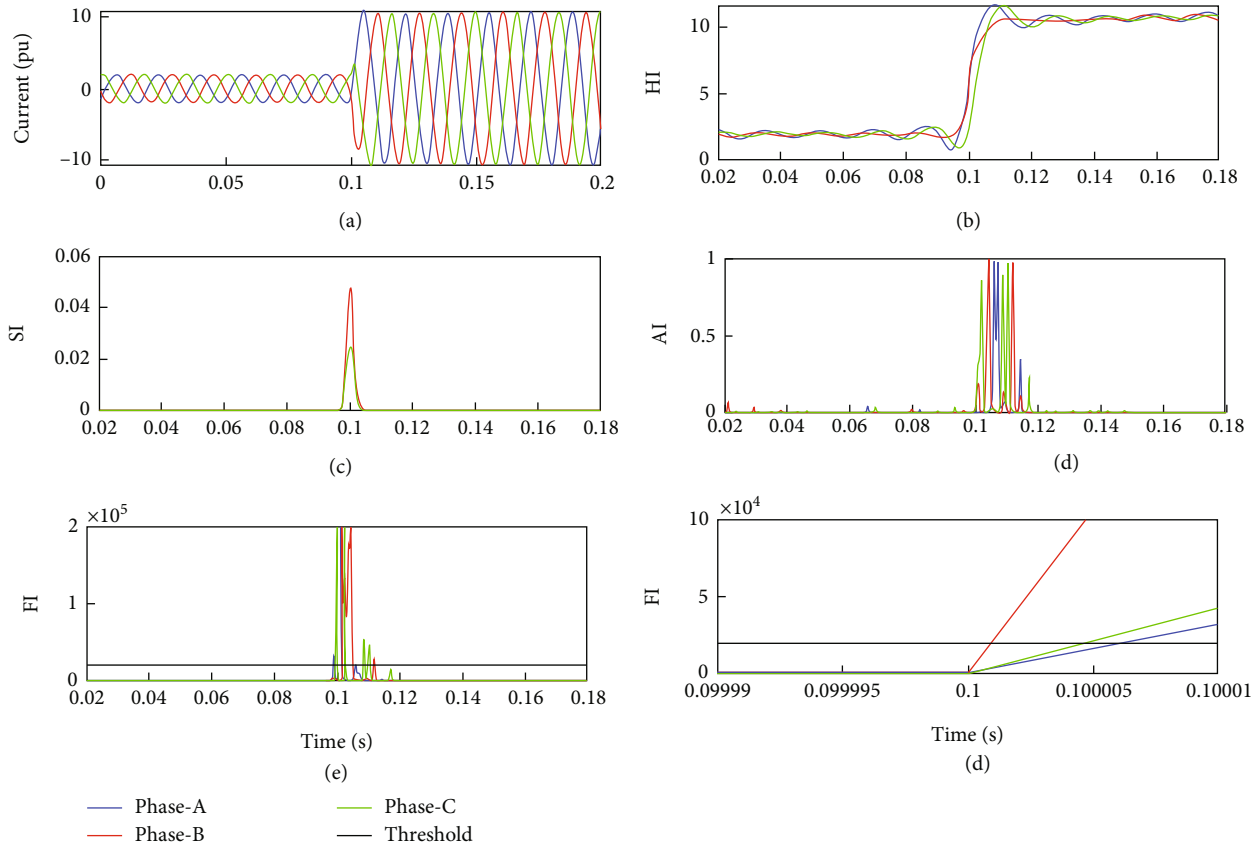

Figure 8: ABCG fault: (a) current waveforms, (b) HI, (c) SI, (d) AI, (e) FI, and (f) high-resolution FI plot.

Table 2: Maximum magnitude of FI of all phases during fault events.

S. no.	Fault type	Phase A	Phase B	Phase C
1	AG	1.8405×10^5	477.08	1735.2
2	AB	1.1602×10^6	1.4206×10^6	7.4807
3	ABG	8.043×10^5	3.5743×10^6	3480.6
4	ABC	8.6227×10^5	8.2113×10^6	4.1432×10^6
5	ABCG	8.6862×10^5	8.1277×10^6	4.7571×10^6

be effectively identified using GFI to differentiate the ABCF and ABCGF faults.

Robustness of the proposed method to classify the different faulty events and discriminate these events from each other is performed by testing the algorithm on 25 data sets of each fault event. The data set is obtained by changing the different parameters such as fault incidence angle, fault resistance, fault location node, and level of RE penetration. Data of accurately classified and inaccurately classified faults are provided in Table 3. After detailed analysis of the results provided in Table 3, it is observed that average fault accuracy above 99% is obtained using the proposed protection algorithm which indicates the robustness of the algorithm.

5. Performance Validation of Protection Algorithm: Case Studies

Performance of the designed protection algorithm has been validated for case studies to generalize and check the robustness of the algorithm to detect fault events during all possible fault and healthy conditions. Simulation results for various cases of study are detailed in this section.

5.1. Fault Impedance Variations. Fault on phase-A with ground (AG) is realized to occur on node 671 of utility system considering fault impedance of 0.01 Ω, 2 Ω, 4 Ω, 6 Ω, 8 Ω, and 10 Ω. The currents pertaining to all phases are measured at PSN for all investigated fault impedance. These currents are analyzed applying the formulated protection approach for computing FI which are recorded in Table 4. Detailed analysis of data shows that FI pertaining with faulty phase-A is high relative to TH. However, FI is lower relative to TH for the phases-B and C (healthy in nature). Hence, the designed protection approach effectively detect the fault incident on the network for fault impedance up to 10 Ω with high share of RE.

5.2. Variations of Fault Incidence Angle. Fault on phase-A with ground (AG) is realized to occur on node 671 of utility system considering fault occurrence angle (FOA) of 0°, 30°, 45°, 60°, 90°, 120°, and 150°. Currents of all phases are

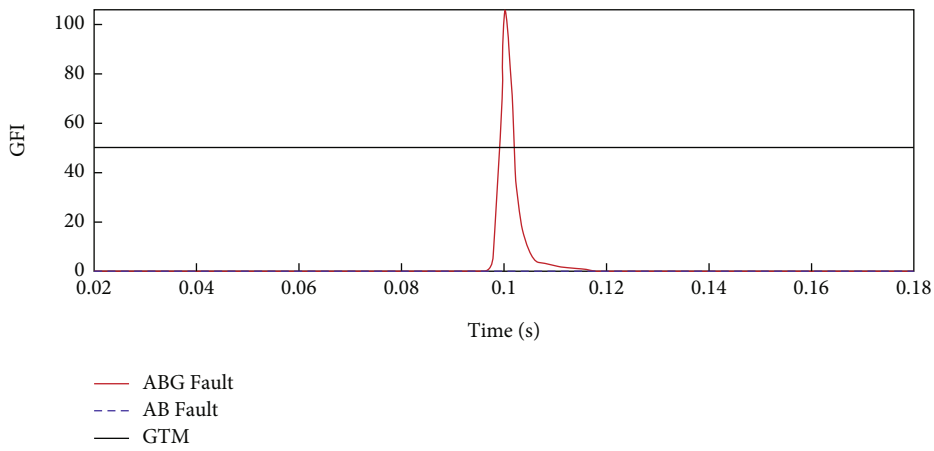

Figure 9: GFI discriminating AB and ABG faults.

Table 3: Data of accurately and inaccurately classified faults.

S. no.	Fault type	Nos. of fault data	Nos. of accurately classified faults	Nos. of inaccurately classified faults	Fault classification efficiency (%)
1	AG	25	25	0	100%
2	AB	25	24	1	96%
3	ABG	25	25	0	100%
4	ABC	25	25	0	100%
5	ABCG	25	25	0	100%
Average fault classification accuracy (%)					99.20%

Table 4: FI during AG fault considering different fault impedance.

S. no.	Phase	Peak of FI with different fault impedance					
		0.01 Ω	2 Ω	4 Ω	6 Ω	8 Ω	10 Ω
1	A	1.8405×10^5	1.3319×10^5	97938	72762	54953	42096
2	B	477.08	365.03	298.05	248.93	216.92	189.14
3	C	1735.2	1166.9	820.84	587.37	481.91	386.49

Table 5: FI during AG fault event for different FOA.

S. no.	Phase	Maximum magnitude of FI with various fault occurrence angles						
		0°	30°	45°	60°	90°	120°	150°
1	A	1.8405×10^5	4.5307×10^5	6.644×10^5	5.7621×10^5	4.1027×10^5	5.7817×10^5	5.0787×10^5
2	B	477.08	3043.4	8334.9	1922	1943	763.58	127.639
3	C	1735.2	1268.1	1111	771.21	281.46	85.744	137.473

measured at PSN for all investigated FOA. The currents are analyzed by application of designed protection approach to compute FI which are recorded in Table 5. Detailed analysis of data shows that FI of phase-A (faulty in nature) is high relative to TH for all investigated FOA. However, FI is low relative to TH for phases-B and C (healthy in nature). Hence, the designed protection approach effectively identified the fault incident on the network for all investigated FOA with high share of RE.

5.3. Performance of Algorithm in Noisy Condition. The AG fault is realized to occur on node 671 of the utility system. Currents associated to all phases are recorded at PSN. Gaussian noise of level of 20 dB signal-to-noise ratio (SNR) is added to these current signals and noisy currents. These current waveforms with noise are illustrated in Figure 10(a). Currents are analyzed by application of the designed protection approach to compute HI, SI, AI, and FI which are shown in Figures 10(b)–10(e) sequentially.

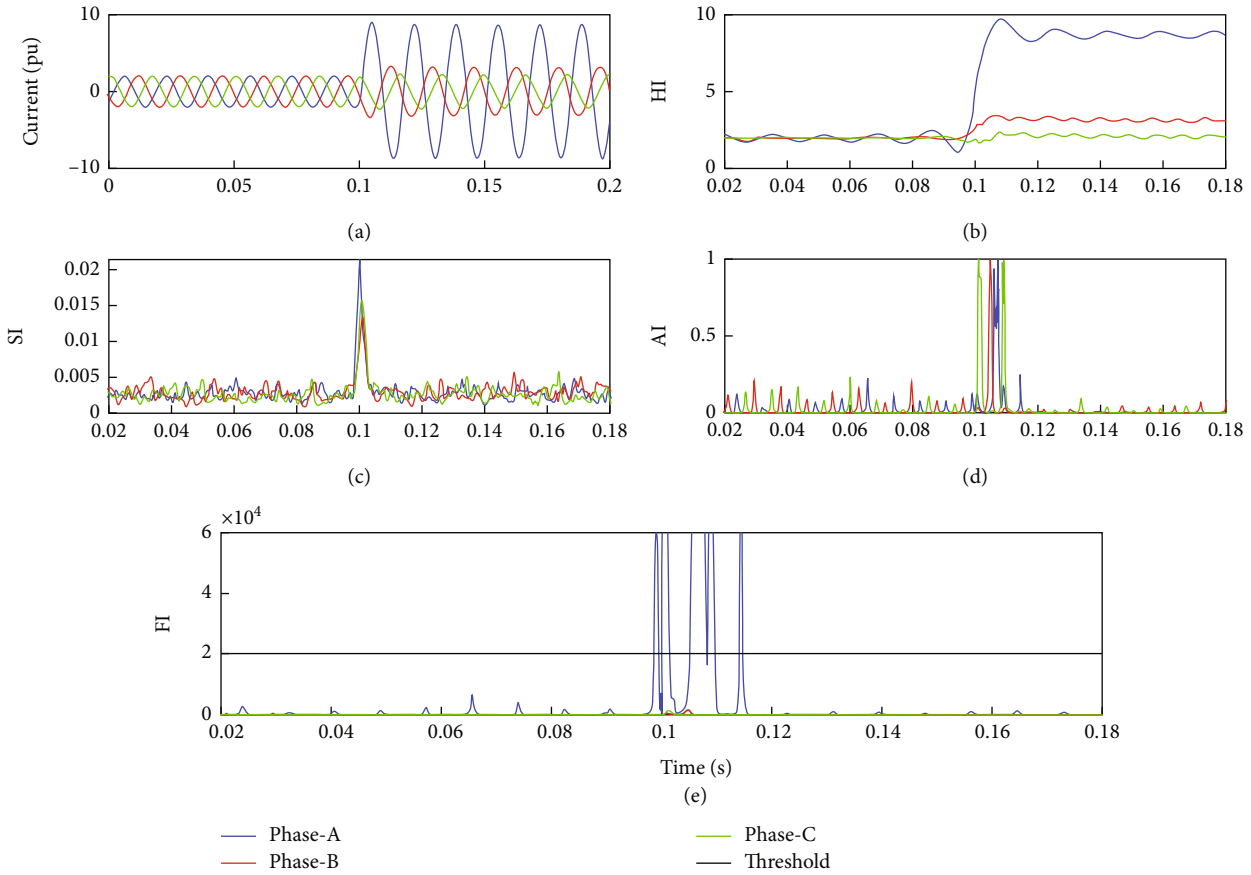

Figure 10: AG fault in noisy condition: (a) current waveforms, (b) HI, (c) SI, (d) AI, and (e) FI.

This is seen in Figure 10(a) that current of phase-A (faulty nature) has increased because of fault occurrence. However, currents of phases-B and C (healthy nature) change by small quantum. Figure 10(b) details that HI of phase-A (faulty nature) has become high due to AG fault. However, change in HI magnitude for phases-B and C (healthy nature) is small. Figure 10(c) depicts that SI pertaining to all phases has become high due to fault incidence. Figure 10(d) shows that AI pertaining to all phases has become high due to AG fault occurrence at 0.1 s. Figure 10(e) describes that FI of faulty phase-A has become high due to AG fault occurrence at 0.1 s and crossed the TH. However, FI for healthy phases-B and C remains below TH. Hence, AG fault event has been determined accurately and effectively in noisy condition.

5.4. Effect of Fault Location on Different Nodes of Test Feeder. Fault on phase-A with ground (AG) is realized at different nodes of the test utility system. Currents pertaining to all phases are recorded at PSN. The currents are analyzed applying the designed protection approach to compute HI, SI, AI, and FI. Peak magnitude of FI for all three phases with AG fault occurred at all nodes is detailed in Table 6. This is seen that for all the fault locations on the test utility network, FI associated to phase-A is high relative to threshold TH (20,000) and FI pertaining with phases-B and C has values lower relative to TH. Hence, it is realized that the designed method is effective for detecting the fault occurred on all the nodes of test grid.

Table 6: Peak Magnitude of FI of All Phases during Fault Events.

S. no.	Fault type	Phase		
		A	B	C
1	671	1.8405×10^5	477.08	1735.2
2	632	2.4581×10^5	502.92	2012.9
3	645	2.3109×10^5	499.05	1992.6
4	646	2.0576×10^5	488.62	1872.1
5	633	2.3218×10^5	490.70	1891.5
6	634	1.0901×10^5	480.99	1765.2
7	692	1.7092×10^5	462.18	1702.8
8	675	1.6054×10^5	443.21	1672.4
9	684	1.7149×10^5	465.64	1698.1
10	611	1.5108×10^5	436.09	1658.4
11	652	1.5098×10^5	421.71	1634.9
12	680	1.6107×10^5	446.01	1678.7

5.5. Load Switching. A load of capacity 843 MW and 462MVAR connected to 675-numbered node is turned off at 4th cycle. This load is again reconnected at 8th cycle.

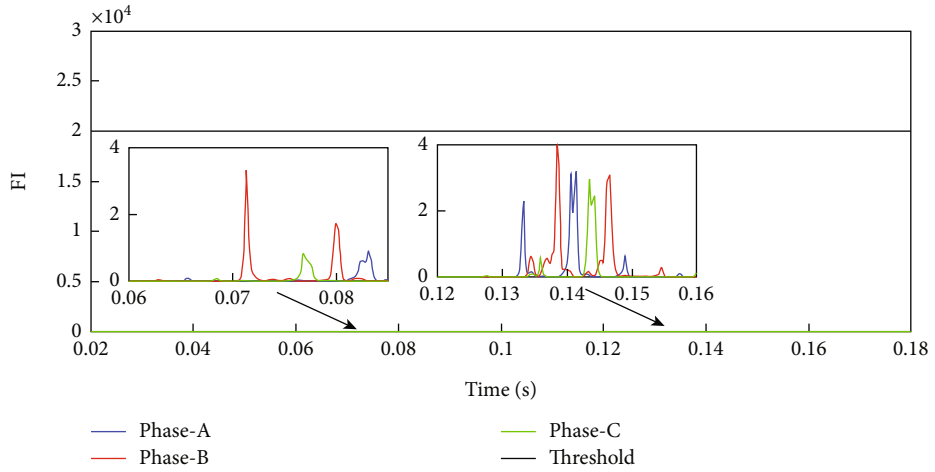

Figure 11: FI with event of switching the load.

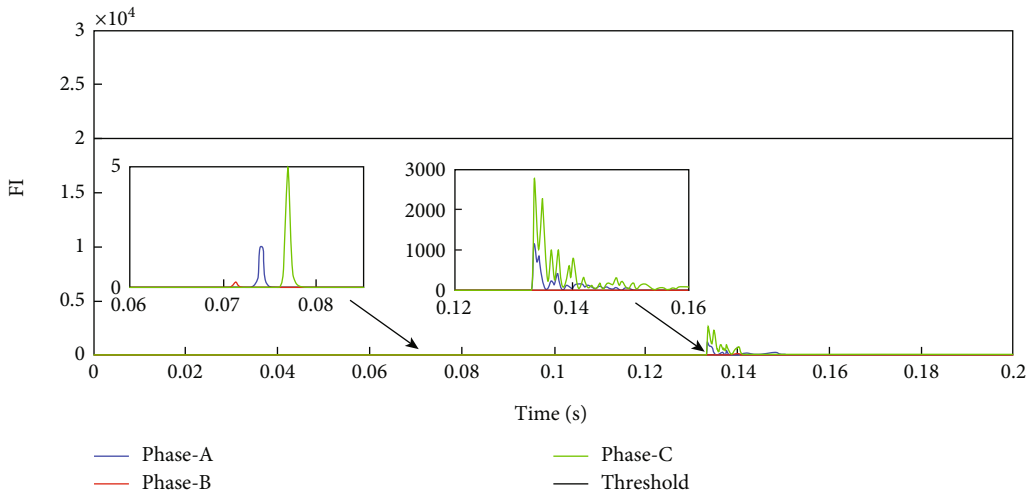

Figure 12: FI with event of capacitor switching.

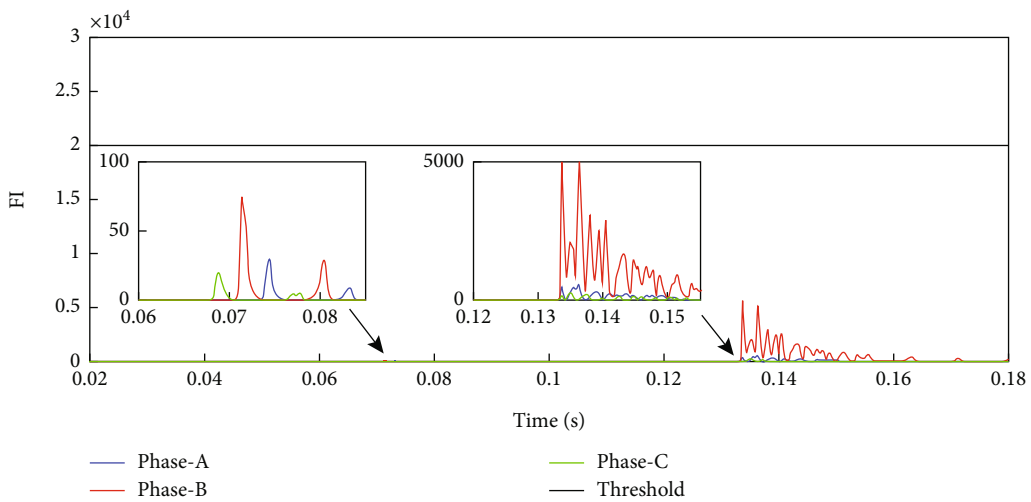

Figure 13: FI with event of feeder operation.

Table 7: Performance comparative study.

S. no.	Parameter of comparative study	Reference [26]	Reference [27]	Proposed method
1	Maximum error of fault detection (%)	9.54	11.27	1.89
2	Sampling frequency (kHz)	Not specified	Not specified	3.84 kHz
3	Fault classification	Investigated	Investigated	Investigated
4	Minimum noise level for which performance is not deteriorated	30 dB SNR	Not investigated	20 dB SNR
5	Effect of loading	Not investigated	Not investigated	Investigated
6	Synchronized data at both ends of line	Required	Not required	Not required
7	Effect of fault angle	Investigated	Not investigated	Investigated
8	Effect of fault resistance	Investigated	Not investigated	Investigated
9	Mean error of fault detection (%)	5.99	6.95	0.978

Currents pertaining to every phase is recorded at PSN. The currents are analyzed applying the designed protection approach to compute FI which is illustrated in Figure 11. This can be seen that FI for all phases has become slightly high at the moment of disconnecting the load as well as reconnecting the load. However, FI is always low in comparison to TH. Therefore, event of load switching is a nonfaulty event and discriminated from the faulty events.

5.6. Capacitor Switching. A capacitor load of capacity 600MVAR connected to 675-numbered node is turned off at 4^{th} cycle. This capacitor is again reconnected at 8^{th} cycle. Current pertaining to every phase is recorded at PSN. The currents are analyzed by applying the designed protection approach to compute FI which is illustrated in Figure 12. This can be seen that FI for all phases has increased at the time of disconnecting the capacitor load as well as reconnecting the capacitor load. However, FI is always lower relative to TH. Therefore, event of capacitor switching is a nonfaulty event and differentiated from faulty events.

5.7. Feeder Tripping. Feeder comprising of 692- and 675-numbered nodes is tripped at 4^{th} cycle. This is reconnected at 8^{th} cycle. The currents pertaining with all phases are recorded at PSN. The currents are analyzed by applying the designed protection approach to compute FI which is illustrated in Figure 13. This can be seen that FI for all phases has increased at the time of disconnecting the feeder as well as reconnecting the feeder. However, FI is always lower relative to TH. Therefore, event of feeder operation is nonfaulty event and discriminated from the faulty events.

6. Performance Comparison

Effectiveness of the designed protection scheme for a utility grid having high RE (wind and solar energy) contribution is tested by comparing performance with an alienation coefficient-based protection schemes (ACPS) discussed in [26] considering the maximum error, mean error, noisy scenario, fault impedance variability, and fault occurrence angle variations. The performance of algorithm is also compared with the discrete wavelet transform- (DWT-) based protection algorithm reported in [27]. This is established that the proposed protection scheme performs efficiently and effectively relative to alienation-based protection approach reported in [26] and DWT-based technique reported in [27]. In a noisy condition, the performance of the alienation protection scheme of [26] has deteriorated with noise levels greater compared to 30 dB SNR whereas the designed protection scheme performs well up to noise level of 20 dB SNR. Impact of noise on the DWT-based protection algorithm has not been investigated. A performance comparison of the designed algorithm, alienation coefficient-based technique, and DWT-based method for fault recognition is included in Table 7.

7. Concluding Remark

A protection scheme for utility grid having high contribution of RE (wind and solar energy) is designed in this paper. This method extracts the current features using ST, HT, and alienation coefficient for fault detection. Fault classification is performed using number of fault phases and a zero sequence current-based GFI.

This is concluded that the protection scheme effectively detect and classify the faults such as AG, AB, ABG, ABC, and ABCG in the presence of 50% RE contribution level in the utility system. The protection scheme is effective to detect faults for different case studies such as variations of fault impedance, variations of fault occurrence angle (FOA), fault incident at different nodes, and noisy condition (20 dB SNR). It is also concluded that the protection scheme effectively discriminates the fault events from operational events such as feeder operation, load, and capacitor switching. The performance of the designed protection approach is superior relative to alienation coefficient-based protection method reported in literature. ACPS has maximum error and mean error of 9.54% and 5.99%, respectively, for fault detection which is high compared to respective values for the proposed method which are 1.89% and 0.978%, respectively. ACPS is effective for detecting fault events in noise level of 30 dB SNR whereas the proposed method effectively identifies the faults in the high noise scenario of 20 dB SNR. The study is performed on the IEEE-13 bus test network which interfaced a solar and a wind power plant. The performance of the proposed method is also superior relative to the DWT-based technique.

Parameters of the proposed protection algorithm can be adjusted using an optimization technique which has been considered the future scope of the research work. Further, hybrid combination of signal processing techniques, artificial intelligent techniques, and optimization techniques may be explored to design intelligent and self-learning-based protection algorithms.

Data Availability

Data will be available on request. For the data-related queries, kindly contact Baseem Khan (baseem.khan1987@gmail.com).

Conflicts of Interest

The authors declare that they have no conflicts of interest.

References

[1] H. Haes Alhelou, M. Hamedani Golshan, and J. Askari Marnani, "Robust sensor fault detection and isolation scheme for interconnected smart power systems in presence of RER and EVs using unknown input observer," *International Journal of Electrical Power Energy Systems*, vol. 99, pp. 682–694, 2018.

[2] W. Elmasry and M. Wadi, "EDLA-EFDS: a novel ensemble deep learning approach for electrical fault detection systems," *Electric Power Systems Research*, vol. 207, article 107834, 2022.

[3] A. Sabat, S. K. Gouda, B. K. Panigrahi, P. K. Sahoo, A. Dash, and P. K. Ray, "Transmission line fault detection in presence of wind turbine using wavelet transform," in *2018 International Conference on Applied Electromagnetics, Signal Processing and Communication (AESPC)*, vol. 1, pp. 1–4, Bhubaneswar, India, 2018.

[4] A. A. Aljabery, H. Mehrjerdi, and A. Iqbal, "Impact of solar and wind energies on distance protection of transmission lines," in *2021 IEEE 4th International Conference on Computing, Power and Communication Technologies (GUCON)*, pp. 1–6, Kuala Lumpur, Malaysia, 2021.

[5] R. Dashti, M. Daisy, H. Mirshekali, H. R. Shaker, and M. Hosseini Aliabadi, "A survey of fault prediction and location methods in electrical energy distribution networks," *Measurement*, vol. 184, article 109947, 2021.

[6] S. Jadidi, H. Badihi, and Y. Zhang, "Fault Diagnosis in Microgrids with Integration of Solar Photovoltaic Systems:A Review," *IFAC-PapersOnLine*, vol. 53, no. 2, pp. 12091–12096, 2020.

[7] M. Shaik, A. G. Shaik, and S. K. Yadav, "Hilbert-Huang transform and decision tree based islanding and fault recognition in renewable energy penetrated distribution system," *Sustainable Energy, Grids and Networks*, vol. 30, article 100606, 2022.

[8] J. O. C. P. Pinto and M. Moreto, "Protection strategy for fault detection in inverter-dominated low voltage ac microgrid," *Electric Power Systems Research*, vol. 190, article 106572, 2021.

[9] A. Srivastava and S. Parida, "Data driven approach for fault detection and Gaussian process regression based location prognosis in smart ac microgrid," *Electric Power Systems Research*, vol. 208, article 107889, 2022.

[10] P. Wang, P. Poovendran, and K. B. Manokaran, "Fault detection and control in integrated energy system using machine learning," *Sustainable Energy Technologies and Assessments*, vol. 47, article 101366, 2021.

[11] K. Piromsopa and R. J. Enbody, "Survey of protections from buffer-overflow attacks," *Engineering Journal*, vol. 15, no. 2, pp. 31–52, 2011.

[12] S. Devi, N. K. Swarnkar, S. R. Ola, and O. P. Mahela, "Detection of transmission line faults using discrete wavelet transform," in *2016 Conference on Advances in Signal Processing (CASP)*, Pune, India, 2016.

[13] L. Zamboni, I. Nunes da Silva, L. Nascimento Soares, and R. A. Souza Fernandes, "Fault detection in power distribution systems using automated integration of computational intelligence tools," *IEEE Latin America Transactions*, vol. 9, no. 4, pp. 522–527, 2011.

[14] F. Mohammadi, G. Nazri, and M. Saif, "A fast fault detection and identification approach in power distribution systems," in *2019 International Conference on Power Generation Systems and Renewable Energy Technologies (PGSRET)*, pp. 1–4, Istanbul, Turkey, 2019.

[15] M. Elsisi and M. Soliman, "Optimal design of robust resilient automatic voltage regulators," *ISA Transactions*, vol. 108, pp. 257–268, 2021.

[16] M. N. Ali, M. Soliman, M. A. Ebrahim, and M. Elsisi, "D-decomposition-based multi-objective robust resilient control for blade pitch of wind energy conversion system," *International Journal of Electrical Power & Energy Systems*, vol. 146, article 108781, 2023.

[17] M. Sadiq, C. A. Aragon, Y. Terriche et al., "Continuous-control-set model predictive control for three-level DC–DC converter with unbalanced loads in bipolar electric vehicle charging stations," *Mathematics*, vol. 10, no. 19, p. 3444, 2022.

[18] M. A. E. Mohamed, S. M. R. Mohamed, E. M. M. Saied, M. Elsisi, C.-L. Su, and H. A. Hadi, "Optimal energy management solutions using artificial intelligence techniques for photovoltaic empowered water desalination plants under cost function uncertainties," *IEEE Access*, vol. 10, pp. 93646–93658, 2022.

[19] M.-Q. Tran, M. Elsisi, V. Q. Vu, F. Albalawi, and S. S. M. Ghoneim, "Effective optimization based on equilibrium optimizer for dynamic cutting force coefficients of the end-milling process," *Mathematics*, vol. 10, no. 18, p. 3287, 2022.

[20] M. Elsisi and M. E. S. M. Essa, "Improved bald eagle search algorithm with dimension learning-based hunting for autonomous vehicle including vision dynamics," *Applied Intelligence*, 2022.

[21] O. P. Mahela, V. S. Bhati, G. Ahmad et al., "A protection scheme for distribution utility grid with wind energy penetration," *Computers Electrical Engineering*, vol. 94, article 107324, 2021.

[22] O. P. Mahela and A. G. Shaik, "Power quality recognition in distribution system with solar energy penetration using _S_ -transform and fuzzy C-means clustering," *Renewable Energy*, vol. 106, pp. 37–51, 2017.

[23] O. P. Mahela and A. G. Shaik, "Power quality detection in distribution system with wind energy penetration using discrete wavelet transform," in *2015 Second International Conference on Advances in Computing and Communication Engineering*, pp. 328–333, Dehradun, India, 2015.

[24] A. Derviskadic, G. Frigo, and M. Paolone, "Beyond phasors: modeling of power system signals using the Hilbert transform," *IEEE Transactions on Power Systems*, vol. 35, pp. 2971–2980, 2019.

[25] O. P. Mahela, A. G. Shaik, B. Khan, R. Mahla, and H. H. Alhelou, "Recognition of complex power quality disturbances using S-transform based ruled decision tree," *IEEE Access*, vol. 8, article 173530, 2020.

[26] B. Rathore and A. G. Shaik, "Alienation based fault detection and classification in transmission lines," in *2015 Annual IEEE India Conference (INDICON)*, pp. 1–6, New Delhi, India, 2015.

[27] A. Kulshrestha, O. P. Mahela, and M. K. Gupta, "A discrete wavelet transform and rule based decision tree based technique for identification of fault in utility grid network with wind energy," in *2021 First IEEE International Conference on Advances in Electrical, Computing, Communications and Sustainable Technologies (ICAECT 2021), Shri Shankarachariya Technical Campus (SSTC)*, Bhilai, Chhattisgarh, India, 2021.